MATERIALS SCIENCE

Growth mechanism of carbon nanotubes from Co-W-C alloy catalyst revealed by atmospheric environmental transmission electron microscopy

Yang Wang[1,2], Lu Qiu[3], Lili Zhang[1]*, Dai-Ming Tang[4]*, Ruixue Ma[1,2], Cui-Lan Ren[5,6], Feng Ding[3,7]*, Chang Liu[1]*, Hui-Ming Cheng[1,8]

High–melting point alloy catalysts have been reported to be effective for the structure-controlled growth of single-wall carbon nanotubes (SWCNTs). However, some fundamental issues remain unclear because of the complex catalytic growth environment. Here, we directly investigated the active catalytic phase of Co-W-C alloy catalyst, the growth kinetics of CNTs, and their interfacial dynamics using closed-cell environmental transmission electron microscopy at atmospheric pressure. The alloy catalyst was precisely identified as a cubic η-carbide phase that remained unchanged during the whole CNT growth process. Rotations of the catalyst nanoparticles during CNT growth were observed, implying a weak interfacial interaction and undefined orientation dependence for the solid catalyst. Theoretical calculations suggested that the growth kinetics are determined by the diffusion of carbon atoms on the surface of the η-carbide catalyst and through the interface of the catalyst-CNT wall.

INTRODUCTION

High–melting point catalysts, especially Co-W alloys, including Co_7W_6 intermetallic and Co-W-C ternary carbides, have shown promise in the structure-controlled growth of single-wall carbon nanotubes (SWCNTs) (*1–14*). The growth mechanism of SWCNTs from the alloy catalysts has been intensively investigated experimentally and theoretically. On the one hand, the selectivity was attributed to the high thermal stability of the solid alloy catalysts and the interface matching between the SWCNTs and the solid catalyst nanoparticles (NPs) (*11–13*). On the other hand, kinetic selectivity mechanism involving the armchair-zigzag (A|Z) edge segregation and transformation has been proposed (*15*, *16*) and supported by a recent experiment, where near (2*n*, *n*) chirality SWCNTs were preferentially grown from three catalysts (W, Mo, and Re) with different symmetries (*17*).

However, up to now, some fundamental but important issues of the Co-W alloy catalyst system, i.e., the actual phase structures and behaviors of the catalysts during CNT growth, the CNT-catalyst interfacial dynamics, and the growth kinetics of CNTs, are still unclear. Although the structures of the alloy catalysts have been investigated, the previous reports are mainly based on postgrowth characterization or in situ characterization of the catalyst NPs without a grown CNT linked (table S1). As a result, the behaviors and structural evolution of the catalysts during CNT growth are still unknown. Yang *et al.* (*11–13*) attributed the selective growth of SWCNTs to the formation of an intermetallic phase of Co_7W_6. By using environmental transmission electron microscopy (ETEM), the Co_7W_6 NPs were observed to be stable under the reactive atmosphere at a high temperature of 1100°C (*18*). On the other hand, An *et al.* (*14*, *19*) reported that the selective growth of SWCNTs from the sputtered Co-W-C catalyst is associated with the formation of a mixture of Co_6W_6C and Co phases, which was identified after SWCNT growth by using atomic-resolution scanning TEM (STEM). In addition to the unclear behaviors of the alloy catalysts during CNT growth, the CNT-catalyst interfacial structure has been rarely studied (*11*, *15*, *16*), especially during the dynamic growth process of CNTs under an environment close to the conventional chemical vapor deposition (CVD) growth system.

In this study, we directly investigated the growth process and mechanism of CNTs from the Co-W-C alloy catalyst NPs in a windowed environmental cell (E-cell) under atmospheric pressure inside a TEM. An aberration-corrected TEM was used to observe the growth of the CNTs and characterize the atomic structures of the catalyst NPs, the dynamic CNT-NP interface, and the growth kinetics of CNTs. On the basis of a precise phase identification method (*20*), the phase structure of the alloy catalyst was found to keep a single phase of cubic ternary carbide (η-carbide) during CNT growth. Unexpectedly, rotations of the solid catalyst NPs inside the growing CNTs were found, implying a weakly bonded CNT-catalyst interface. Density functional theory (DFT)–based calculations showed that carbon diffusion on the ternary carbide surface and through the interface determines the growth kinetics.

[1]Shenyang National Laboratory for Materials Science, Institute of Metal Research (IMR), Chinese Academy of Sciences, 72 Wenhua Road, Shenyang 110016, China. [2]School of Materials Science and Engineering, University of Science and Technology of China (USTC), 72 Wenhua Road, Shenyang 110016, China. [3]Center for Multidimensional Carbon Materials, Institute for Basic Science, Ulsan 44919, South Korea. [4]International Center for Materials Nanoarchitectonics (MANA), National Institute for Materials Science (NIMS), Namiki 1-1, Tsukuba, Ibaraki 305-0044, Japan. [5]Shanghai Institute of Applied Physics, Chinese Academy of Sciences, Shanghai 201800, China. [6]Key Laboratory of Interfacial Physics and Technology, Chinese Academy of Sciences, Shanghai 201800, China. [7]School of Materials Science and Engineering, Ulsan National Institute of Science and Technology, Ulsan 44919, South Korea. [8]Institute of Technology for Carbon Neutrality, Shenzhen Institute of Advanced Technology, Chinese Academy of Sciences, 1068 Xueyuan Road, Shenzhen 518055, China.
*Corresponding author. Email: zhangll@imr.ac.cn (L.Z.); tang.daiming@nims.go.jp (D.-M.T.); f.ding@unist.ac.kr (F.D.); cliu@imr.ac.cn (C.L.)

RESULTS

TEM image simulations of the CNTs and catalyst NPs in an E-cell

A windowed E-cell system was used to investigate the growth of CNTs under atmospheric pressure, in which two amorphous SiN_x membranes separate the reactor from the vacuum of the TEM chamber and a high temperature over 1000°C could be obtained by using the microscale heating circuit on the chip (Fig. 1A). Compared with windowless ETEM at low pressures (<10 mbar), there is a concern that the contrast and resolution may be compromised using the E-cell with a pressure up to 1000 mbar, especially for the thin nanotubes composed of low-density carbon.

To evaluate the experimental feasibility, TEM image simulations were carried out for the E-cell with CNTs and metal catalyst NPs loaded on amorphous SiN_x membranes (Fig. 1, B and C, and figs. S1 to S5). The parameters of the simulated high-resolution TEM (HRTEM) images and diffractograms are summarized in table S2. The presence of the SiN_x membrane obviously reduces the imaging contrast of the CNTs, especially as the membrane thickness is increased (figs. S1 and S3). Nevertheless, the walls of CNTs with diameters larger than 2 nm can be resolved for a 30-nm-thick SiN_x membrane, although it is not possible to resolve their atomic structures by HRTEM or chiral structures by electron diffraction (Fig. 1C and fig. S2, B to D and F to H). On the other hand, the atomic structures of the catalyst NPs could be resolved because of their larger electron scattering cross section (Fig. 1C and fig. S2, J to L and N to P).

Atomic resolution of the metallic catalysts has been confirmed by preliminary experimental results (Fig. 1, D and E). A lattice-resolved TEM image and the corresponding fast Fourier transformation (FFT) pattern could be seen for a Co-W-C catalyst NP that is attached to the end of a triple-wall CNT (TWCNT). Therefore, the E-cell system is suitable for observing the growth process of the CNTs and for investigating the atomic structures of the catalysts during CNT growth even under atmospheric pressure.

Preparation and characterization of Co-W-C alloy catalyst

Catalyst NPs were prepared by successively sputtering Co and W thin films on the bottom SiN_x membrane of the E-cell (*20*), followed by a heat treatment at 850°C in H_2 atmosphere for 10 min. Figure S6 shows the typical morphology of the as-prepared catalyst NPs. The catalyst NPs are spherical, and their diameters are mainly distributed in the range of 2 to 6 nm, with a mean diameter of 4.2 nm (fig. S6). It was found that the prepared catalyst NPs were mainly a cubic Co-W-C η-carbide phase (Fig. 2 and fig. S7) due to the carbonaceous residue, while some hexagonal Co_7W_6 intermetallic NPs could be obtained after long-time gas surging in a few cases (fig. S8). In addition, the catalyst NPs were found to be η-carbides under the growth condition of the CNTs of mixed C_2H_4 and H_2 at atmospheric pressure.

In Fig. 2A, the lattice of a Co-W-C with a diameter of 5.1 nm is resolved. Diffraction spots corresponding to (33-3) and (4-40) planes are identified in the FFT pattern (Fig. 2B), and the catalyst could be indexed as the η-carbide phase along [112] zone axis. The HRTEM image and FFT pattern are consistent with the simulated image and pattern (Fig. 2, C to F). Energy-dispersive x-ray spectroscopy (EDS) maps (fig. S7, J and K) show that Co and W are evenly distributed in the Co-W-C catalyst NPs. Detailed characterization results are summarized in table S3. The measured d-spacings and interplanar angles from the FFT patterns of the catalyst NPs are well fitted to the ternary η-carbide phase with the typical errors within 5% for the d-spacings and 1.2° for the angles.

Phase structure of Co-W-C alloy catalyst during CNT growth

The obtained Co-W-C alloy NPs were used as the catalyst for the growth of CNTs in the windowed E-cell, and the growth process was observed in situ by TEM. After the temperature was increased to 850°C in a 1000 mbar H_2 atmosphere, a mixture of C_2H_4 [0.1 standard cubic centimeter per minute (sccm)] and H_2 (1 sccm) was introduced into the E-cell to initialize CNT growth (fig. S9). The series of HRTEM images in Fig. 3 (A to E) show that a SWCNT grows from a Co-W-C catalyst NP. During the growth, the NP position was fixed, while the growth direction of the CNT

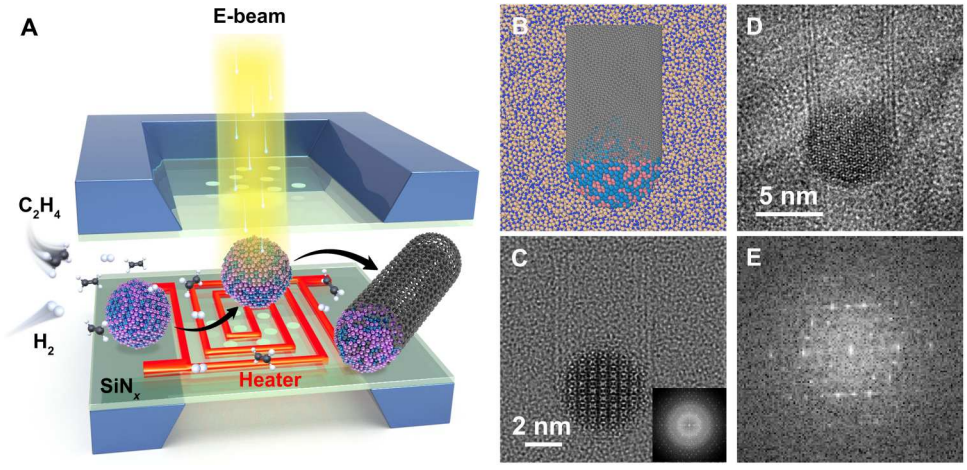

Fig. 1. Schematic and TEM image simulations of TWCNT-NP in an E-cell. (**A**) Schematic showing the cell structure and CNT growth process. E-beam, electron beam. (**B**) Top view of the structural model of a TWCNT attached to a spherical Co_3W_3C NP with a diameter of 5 nm situated on a 30-nm-thick SiN_x membrane. (**C**) Simulations of the HRTEM image and corresponding diffractogram of the TWCNT–Co_3W_3C NP in (B). (**D** and **E**) Experimental HRTEM image and corresponding diffractogram of a TWCNT growing from a cubic Co-W-C NP in the E-cell.

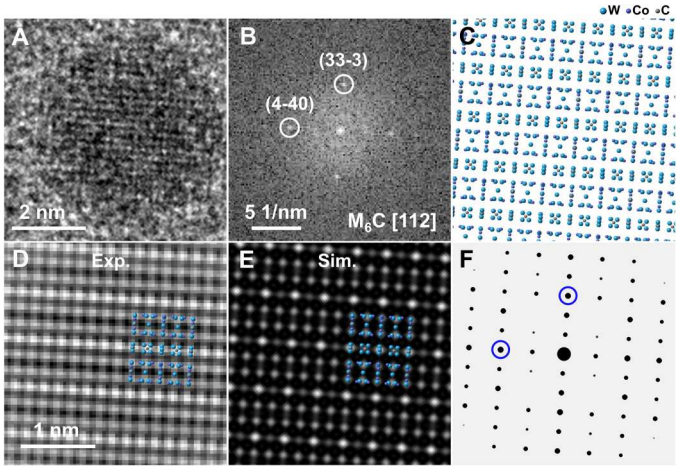

Fig. 2. Structural characterization of the prepared Co-W-C alloy NPs. (**A**) Typical HRTEM image of the prepared Co-W-C NPs. (**B**) FFT patterns of the NP with the phase and zone axis marked. (**C** to **F**) Structure model, Fourier-filtered HRTEM image, simulated HRTEM image, and electron diffraction pattern of the Co-W-C NP along the [112] zone axis taking Co_2W_4C as an example.

was changed from time to time, indicating a base growth mode. The SWCNT maintained a tangential connection to the surface of the catalyst NP (movie S1). In addition to SWCNTs (fig. S10 and movie S2), few-wall CNTs (FWCNTs) with different numbers of walls were also found to have grown from the solid alloy NPs by the tangential growth mode (figs. S11 to S14 and movies S3 to S5). The crystalline structures of the catalyst NPs were analyzed by measuring the FFT patterns from the HRTEM images (Fig. 3, F to J, and figs. S10 to S14) and comparing with the simulations (Fig. 3, K to P, and figs. S10 to S14). They were identified as single-phase η-carbides (table S3), which remained unchanged during the growth of the CNT, while their zone axes kept on changing. In addition, the active phase was found to be the same for the catalyst NPs with different sizes to grow CNTs with different numbers of walls.

The phase structure of the catalyst NPs was further analyzed in a statistical approach. One of the major challenges in identifying the active phase of the Co-W-C catalyst is that there are many phases with similar structures and lattice constants, such as cubic M_6C ($Co_{2+x}W_{4-x}C$, x = 0, 1, 2, η-carbides), cubic $M_{12}C$ (Co_6W_6C, η-carbide), and hexagonal CoW_3C ($Co_3W_{9+x}C_{4-x}$, κ-phase) (*21*–*25*). The lattice parameters of the cubic η-carbides are very close, being 11.21, 11.112, 11.01, and 10.90 Å for Co_2W_4C, Co_3W_3C, Co_4W_2C, and Co_6W_6C, respectively.

On the basis of the precise phase identification method that we developed earlier (*20*), two η-carbides, including cubic M_6C ($Co_2W_4C/Co_3W_3C/Co_4W_2C$) and $M_{12}C$ (Co_6W_6C) phases, for the Co-W-C alloy catalyst during CNT growth were analyzed, and the results are summarized in table S3 and plotted in fig. S15. It can be seen that all the η-carbides are within a reasonable error range (<5% for d-spacing and <2° for angle). The M_6C phases have smaller errors than the $M_{12}C$, and the order of the errors is $Co_3W_3C/Co_4W_2C/Co_2W_4C < W_6Co_6C$, i.e., $M_6C < M_{12}C$. Such results are consistent with the structure characterizations of the catalyst NPs after CVD growth of CNTs (figs. S16 and S17 and table S4). The crystalline structures of the inactive catalyst NPs were also analyzed and found to be the same as that of the active catalyst NPs (fig. S18). We noticed that a few NPs are identified as hexagonal $Co_3W_9C_4$ after the CVD process (fig. S19 and table S5). Such phase was not identified during the in situ growth of CNTs, indicating that it might be formed during the cooling process after CVD growth.

Therefore, the most probable active phase of the Co-W-C catalyst for growing CNTs is identified as a M_6C-type η-carbide phase. Note that the d-spacing difference between M_6C and $M_{12}C$ is within 3% (figs. S15 and S17), which is difficult to strictly distinguish by TEM imaging especially under the dynamic growth conditions. Therefore, at the current stage, we could not strictly exclude the possibility of the coexistence and fluctuation of the M_6C and $M_{12}C$ phases.

Rotation of Co-W-C alloy catalyst during CNT growth

The interface structure between the catalyst and the grown CNT is one of the essential issues for understanding the growth mechanism. From our observations, the Co-W-C catalyst NPs showed high stability regarding the physical state and particle shape. The alloy NPs showed little deformation at 850°C, which is distinct from the traditional transition metal catalysts (Fe, Co, and Ni) (*20*, *26*–*31*). However, it was found that the orientations of the alloy NPs changed dynamically during the SWCNT growth. As shown in Fig. 3, the initial catalyst NP changed its orientation from [491] to [372] by 8.9° at 28.5 s (Fig. 3, F, G, K, and L). After 27.5 s, its orientation rotated 5.4° from [372] to [131] (Fig. 3, H and M) around the [2-24] direction, as shown in the diagram (Fig. 3Q). It then changed to [-4 11 3] and [141], with the shared crystal planes (4-22) and (-1-15) remaining unchanged (Fig. 3, H to J and M to O). Rotations of the catalyst NPs were also observed during the growth of FWCNTs (Fig. 4 and figs. S20 and S21).

On the basis of the statistical analysis of the images of Co-W-C alloy NPs during CNT growth, we found that the shared crystal planes remaining unchanged are frequently the {511}, {422}, and {331} families with a total probability of up to 67.5%, as shown in table S6. In other words, the catalyst NPs tend to rotate around the ⟨511⟩, ⟨422⟩, and ⟨331⟩ crystallographic directions during CNT growth. From the powder diffraction patterns of the cubic Co-W-C ternary carbides (fig. S22), it can be seen that {511}, {422}, and {331} planes are among the four strongest peaks of M_6C (Co_2W_4C/Co_3W_3C), and this may explain why these planes are more frequently observed.

For these NPs without carbon coverage, we found that their orientations rarely changed in the reaction atmosphere even under electron beam irradiation at high temperature for a long time (fig. S23), which rules out the influence of the electron beam for the observed rotations. Therefore, the rotations of the catalyst NPs were mainly attributed to their interactions with the growing CNTs. From postgrowth structure characterizations, changes of the crystalline orientation of the catalysts have been analyzed and attributed to the stress induced by graphitic layers (*32*, *33*). From our in situ observations, it was noticed that the carbon layers could precipitate in an asymmetrical manner, when a catalyst NP was rotating (fig. S24). This asymmetrical precipitating behavior of the carbon layers may cause inhomogeneous interface interaction and the rotation of the catalyst NP.

It was also observed that the growing CNTs rotated frequently with one end attached to the catalyst NPs. The relationship

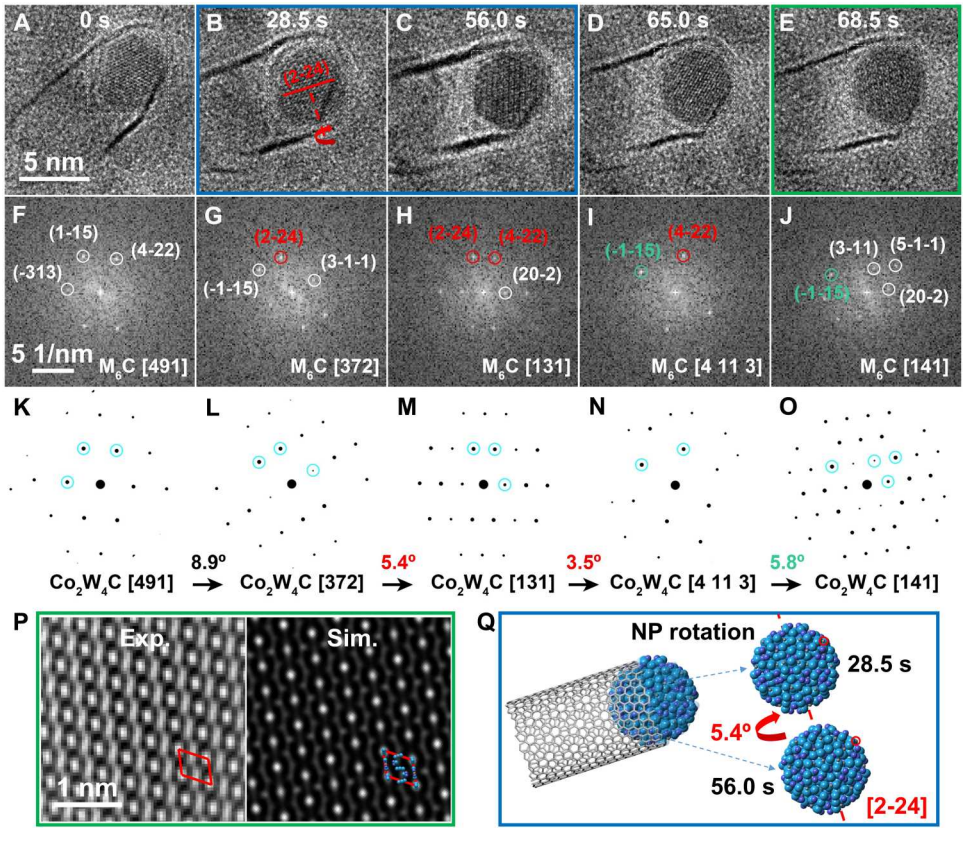

Fig. 3. Structural characterization of a Co-W-C alloy NP during SWCNT growth. (**A** to **E**) Typical HRTEM images of the NP during the growth of a SWCNT. (**F** to **J**) FFT patterns of the NP in (A) to (E), with the corresponding phase and zone axes marked. (**K** to **O**) Simulated electron diffraction patterns with the same zone axes in (F) to (J) taking Co_2W_4C as an example, while the corresponding crystal planes are marked in cyan circles. (**P**) Fourier-filtered HRTEM image and simulated HRTEM image of the NP along the orientation in (E) taking Co_2W_4C as an example. (**Q**) Atomic model diagrams of the NP showing the rotation of the catalyst NP in (B) and (C). The rotation direction of the NP is shown with a red curved arrow, and the practical rotation angle has been magnified by 10° for a better comparison. The reference C atoms are marked in red circles.

between the rotations of the catalyst NPs and the CNTs was analyzed. It was found that they did not necessarily occur at the same time, i.e., the NPs may rotate while the CNTs did not (fig. S25), or that the orientations of the NPs remained unchanged while the CNT rotated (fig. S26). In addition, they did not rotate around the same axis. For instance, within 18.5 s, one catalyst NP changed its orientation from [-102] to [-6 1 11] by 5.0° around the [422] direction while the CNT rotated around the normal direction of the substrate (Fig. 4, A, B, E, F, I, and J), as is shown in the diagram (Fig. 4M). During another period, the catalyst rotated from [-419] to [-529] by 7.2° around the [331] direction (Fig. 4, C, D, G, H, K, L, and N), and it was found that the range and speed of the movements of the NP and the CNT differed a lot. The rotation angles of the NP and the CNT as a function of time are plotted in fig. S27. The CNT rotated continuously within a large angle range (-30° to 30°). On the other hand, the rotation of the catalyst NP is much slower. From the plot, it is interesting to notice that the rotation period of the CNT seems related to the period of the NP rotation. When the rotation of the CNT completed a period at around 6 s, the NP was observed to start to rotate from [-419] zone axis to [-529]. The timing indicates that the rotations of the NP and the CNT are correlated, which is a reasonable result of the asymmetrical precipitation behavior and inhomogeneous interface reaction (fig. S24).

The rotations of the catalyst NPs indicate a weak interfacial interaction between the catalyst NPs and the CNTs, which is different from the previous understanding for the solid catalysts that there should be highly stable CNT-NP interfaces that serve as templates for the structural epitaxial growth of CNTs. From the statistics on the interfacial orientation relationship of the NPs and the CNTs during CNT growth, no fixed relationship could be found between the growth directions of the CNTs and the crystallographic orientations of the catalyst NPs (figs. S28 to S30 and table S7).

Growth kinetics of CNTs from Co-W-C solid alloy catalyst

The growth kinetics of CNTs play an important role in determining their structures (*34*, *35*). In situ TEM examination of the growth of CNTs has been used to investigate the kinetics of CNT growth from traditional transition metal NPs (*30*, *36*–*38*). We found that the growth kinetics of CNTs using Co-W-C solid alloy catalyst is quite different from that using transition metal catalysts. The CNTs grown from the high–melting point alloy catalyst followed a base growth mode at atmospheric pressure, in contrast with the commonly observed tip growth mode for the pure Co catalyst under atmospheric pressure (fig. S31). There were fluctuations for

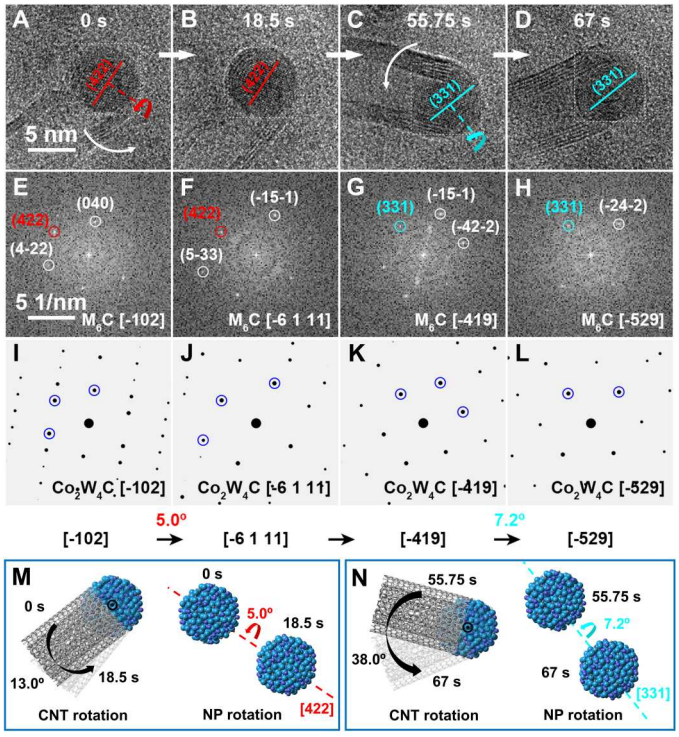

Fig. 4. Rotation of a Co-W-C alloy catalyst NP during CNT growth. (**A** to **D**) Time sequence HRTEM images of the NP during CNT growth. The rotation directions of the CNT are shown with white curved arrows, and the rotation directions of the NP are shown with red and cyan curved arrows. (**E** to **H**) FFT patterns of the NP in (A) to (D). (**I** to **L**) Simulated electron diffraction patterns with the same zone axes in (E) to (H) taking Co_2W_4C as an example. The corresponding crystal planes are marked in blue circles. (**M**) Atomic model diagrams of the CNT-NP showing the rotations of the CNT and the catalyst NP in (A) and (B). (**N**) Atomic model diagrams of the CNT-NP showing the rotations of the CNT and the catalyst NP in (C) and (D). The rotation directions of the CNT are shown with black curved arrows, and the rotation directions of the NP are shown with red and cyan curved arrows. The practical rotation angles of the NP models in (M) and (N) have been magnified by 10° for a better comparison.

the growth of the CNTs from the Co-W-C catalyst NPs (movies S6 and S7). This incubation phenomenon has been observed in other catalyst systems before (*30*, *36*, *37*, *39*). The average growth velocity of the CNTs from the Co-W-C catalyst was measured to be 2 to 5 nm/s (fig. S32), which is about two orders of magnitude slower than that for the Co catalyst (fig. S31). Such a huge difference in the growth velocity shows that the composition of catalyst is an important factor affecting the growth kinetics and structure of CNTs.

To better understand the growth kinetics, the diffusion process was theoretically investigated on the basis of the experimentally identified phase structure of the active catalyst NPs (Fig. 5A). Bulk diffusion in a solid carbide catalyst occurs by vacancy diffusion, and the carbon diffusion activation energy is as high as 2.67 eV (Fig. 5B), which makes it difficult to support the growth of CNTs. This indicates that the carbon supply for CNT growth must take other diffusion paths, i.e., surface diffusion and interface diffusion. We took the (111) plane as a representative plane to estimate the activation energy of surface diffusion in the DFT calculations. As shown in the calculation results (Fig. 5C and fig. S33A), the activation energy for carbon surface diffusion on the (111) plane of a Co_3W_3C solid catalyst is 1.47 eV for [-110] direction and 1.66 eV for [-1-12] direction, which would guarantee the supply of carbon atoms for the growth of SWCNTs and the outermost wall of FWCNTs. For FWCNTs, the carbon supply for the growth of the inner walls must be achieved by interface diffusion, where surface carbon atoms reach the inner walls by crossing the CNT-NP interface (*20*). The activation energies for interface diffusion were calculated to be 1.66 eV at the zigzag edge–Co_3W_3C interface (Fig. 5D) and 2.04 eV at the armchair edge–Co_3W_3C interface (fig. S33B). These energies are much lower than the abovementioned bulk diffusion activation energies. The activation energies for both surface diffusion and interface diffusion on Co_3W_3C are much larger than that for solid Co_3C ($E^* \approx 1$ eV) (*20*), which could lead to orders of magnitude difference in the carbon flux on the catalyst surface and may affect the growth velocity of CNTs greatly. Estimation of the diffusion-limited growth velocity (Supplementary Text) shows that surface and interface diffusion could supply enough carbon atoms for CNT growth.

DISCUSSION

The growth process of CNTs from Co-W-C solid alloy catalyst at atmospheric pressure was investigated by using a windowed gas cell in a Cs-corrected TEM. The active phase of Co-W-C catalyst was identified to be a single-phase cubic η-carbide phase that remained unchanged during CNT growth. Rotations of the catalyst NPs were observed, indicating a weak interfacial interaction between the solid catalyst and the growing CNTs. This fact suggests that it may be difficult to achieve the structure-controlled growth of CNTs solely relying on the structural template function of the solid alloy catalyst, while there is no fixed orientation relationship between the catalyst NPs and the growing CNTs. The growth rate of the CNTs from the alloy catalyst was found to be two orders of magnitude slower than that from the pure Co catalyst, which shows that the growth kinetics of CNTs are related to the composition of the catalyst. DFT calculations showed that the supply of carbon atoms for CNT growth from the solid alloy catalyst is through the surface and interface diffusion.

MATERIALS AND METHODS

Preparation of catalyst

The Co-W-C alloy catalyst NPs were prepared by ion sputtering. Metallic Co and metallic W with certain nominal thickness ratios (Co:W = 0.2 nm:0.3 nm, 0.4 nm:0.6 nm, and 0.3 nm:0.7 nm) were sequentially deposited by an ion sputtering coater (Gatan 681) onto the bottom chip of the windowed E-cell system. The catalyst film supported on the chip was then annealed at 850°C in a H_2 atmosphere for 10 min to form Co-W-C alloy catalyst NPs.

Ex situ characterization of the prepared catalyst

To conduct the EDS analysis of the prepared Co-W-C alloy catalyst, Co and W with thickness ratios (Co:W = 0.4 nm:0.6 nm and 0.3 nm:0.7 nm) were sputtered onto a SiN_x micrograte (from CleanSiN) followed by 10 min of annealing at 850°C in a H_2 atmosphere. High-angle annular dark-field (HAADF)–STEM and EDS mapping were carried out on a TEM (300 kV, FEI Titan Themis) with a Cs probe corrector and a HAADF detector.

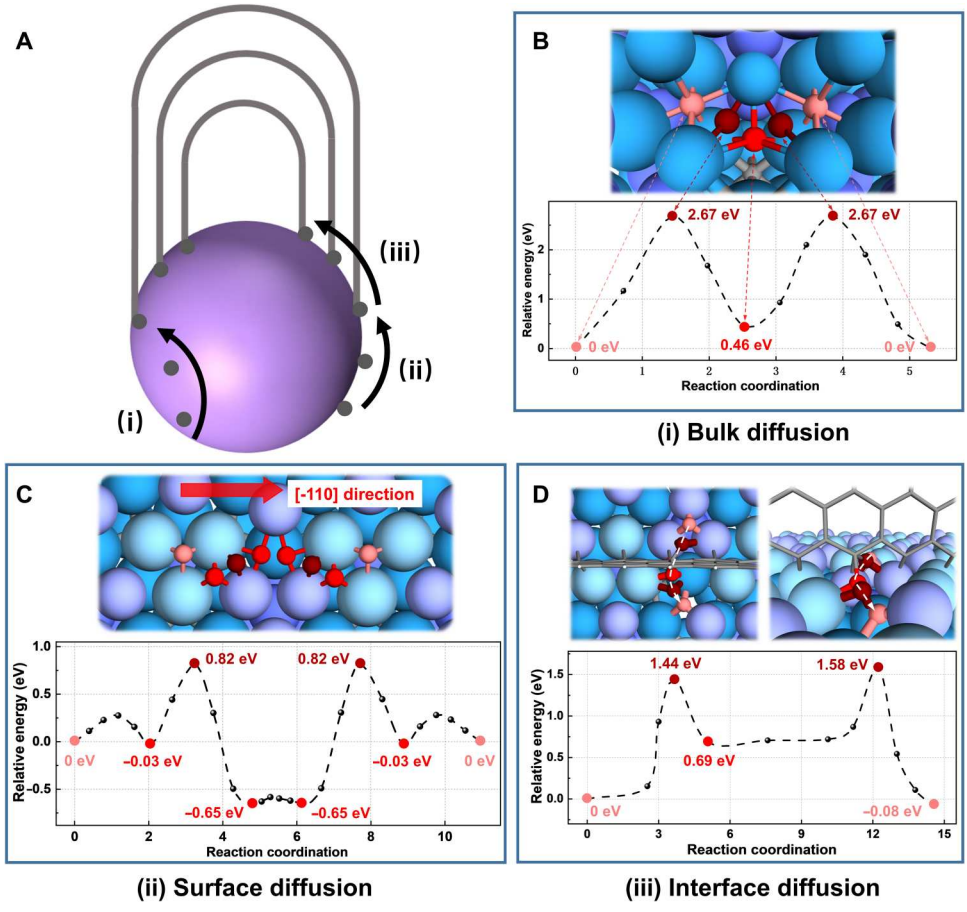

Fig. 5. Calculations of the diffusion paths for CNT growth from Co-W-C alloy catalyst. (**A**) Diagram showing the three possible paths for carbon diffusion during CNT growth from a solid alloy catalyst: (i) bulk, (ii) surface, and (iii) interface. (**B**) Top view of the bulk diffusion process and the minimum energy path (MEP) in a Co_3W_3C solid NP. (**C**) Top view of the surface diffusion process and the corresponding MEP in the [-110] direction for Co_3W_3C (111) plane. (**D**) Top and perspective views of the interface diffusion process between a zigzag CNT edge and the Co_3W_3C surface and the corresponding MEP. Cyan spheres represent W atoms, and purple spheres represent Co atoms. The gray, pink, red, and dark red spheres all denote C atoms, where the pink spheres are the C atoms at the initial and final states, the red spheres are C atoms in intermediate states, and the dark red spheres are C atoms in transition states, corresponding to those in the MEP figures.

In situ TEM experiment

A windowed E-cell system (DENSsolutions Climate S3+) (including a sample holder with a closed cell, a gas supply system, and a heating control unit) was used to conduct the in situ TEM experiments. The reaction cell is made up of a bottom chip, a top chip, and O-rings serving as a micro–CVD assembly for CNT growth. Two SiN_x windows of 30 nm thickness on the top and bottom chips allow the electron beam to pass through and serve as an observation window. The maximum temperature is 1000°C, and the maximum pressure is 1000 mbar. A Cs-corrected TEM (FEI Titan Themis) operated at 300 kV was used to observe the growth of the CNTs. The screen current was set as 2 to 2.5 nA (with a corresponding dose rate of about 3.6×10^3 to 7.4×10^3 e/Å^{2}s). A Ceta camera was used to acquire the TEM images and movies, and the exposure time was set as 0.25 to 1 s. A mixture of C_2H_4 and H_2 (with a corresponding flow rate ratio = 0.1 sccm:1 sccm to 0.2 sccm:1 sccm) was introduced into the E-cell system for CNT growth. The growth temperature was set as 850°C, and the growth pressure was 1000 mbar.

Ex situ growth of CNTs in CVD

Co and W were sequentially sputtered onto the SiN_x micrograte with thickness ratios of 0.2 nm:0.3 nm and 0.3 nm:0.7 nm. The grids were then transferred into a tubular furnace, followed by a reduction pretreatment at 850°C for 10 min to form Co-W-C alloy catalyst NPs. C_2H_5OH was used as the carbon source, and a mixture of C_2H_5OH (Ar)/H_2 (flow rate = 30 sccm:60 sccm) was introduced into the furnace for CNT growth. The growth temperature was 850°C, and growth time was 10 to 15 min.

Phase identification

The crystal planar spacings (d_1, d_2, and d_3) and corresponding interplanar angles (θ_{12} and θ_{23}) were measured from the FFT patterns transformed from the HRTEM images. The measured d-spacings and angles were then compared with the standard data of candidate phases in the Inorganic Crystal Structure Database (ICSD). The information for Co_4W_2C was obtained from SpringerMaterials. The structure data of Co_7W_6 were obtained from the Automatic FLOW (AFLOW) database.

Electron diffraction pattern simulation

The crystal models were constructed by using CrystalMaker and VESTA based on the CIF files of the phases acquired from the ICSD. The simulated electron diffraction patterns were obtained using SingleCrystal combined with CrystalMaker. The crystal thickness was set as 10 nm, and accelerating voltage was set at 300 kV, consistent with the operating voltage for observation.

HRTEM image simulation

The amorphous SiN_x models were acquired by the molecular dynamics calculation with a rapid cooling process being carried out on the melted Si_3N_4 materials (which were constructed by randomly packing atoms with a specified atomic ratio of Si/N). The structural models of the CNTs, Au, Co, Co_7W_6, and Co_3W_3C NPs for TEM image simulations were built using Materials Studio. HRTEM image simulations for the CNTs and metal NPs were performed using the Quantitative STEM simulation package (*40*). The voltage was set as 300 kV, and the spherical aberration C_3 value was set as 0.001 mm for the CNTs, Au, Co, Co_7W_6, and Co_3W_3C NPs and 1 mm for the Co_2W_4C NPs. The slice thickness was set as around 1 Å (with the total number of slices ranging from 200 to 500). The convergence angles for the simulations of metal NPs (Au, Co, Co_7W_6, and Co_3W_3C and Co_2W_4C) were set as 1 mrad, and the convergence angles for the CNTs or CNTs attached to Au and Co_3W_3C NPs were set as 10 mrad, to obtain the best imaging contrast.

DFT calculation

DFT calculations were performed using the Vienna Ab initio Simulation Package (VASP) (*41–43*) with the projected augmented wave method (*44*) and the generalized gradient approximation for the exchange-correlation interactions (*45*). The Brillouin zone was sampled with different Monkhorst-Pack mesh *k*-points with a separation criterion of 0.02 (*46*). Criteria for energy and force convergence were 10^{-4} eV and 10^{-2} eV/Å, respectively. The diffusion barriers were calculated using the climbing image nudged elastic band method (*42*, *44*, *47*) with a 400-eV plane-wave cutoff energy. The calculations of the free energies for the phase diagram were performed using Phonopy (*48*, *49*) and VASP with a 600-eV plane-wave cutoff energy.

Supplementary Materials

This PDF file includes:
Supplementary Text
Figs. S1 to S33
Tables S1 to S7
References

Other Supplementary Material for this manuscript includes the following:
Movies S1 to S7

REFERENCES AND NOTES

1. S. M. Bachilo, L. Balzano, J. E. Herrera, F. Pompeo, D. E. Resasco, R. B. Weisman, Narrow (*n*,*m*)-distribution of single-walled carbon nanotubes grown using a solid supported catalyst. *J. Am. Chem. Soc.* **125**, 11186–11187 (2003).
2. G. Lolli, L. Zhang, L. Balzano, N. Sakulchaicharoen, Y. Tan, D. E. Resasco, Tailoring (*n*,*m*) structure of single-walled carbon nanotubes by modifying reaction conditions and the nature of the support of CoMo catalysts. *J. Phys. Chem. B* **110**, 2108–2115 (2006).
3. X. Li, X. Tu, S. Zaric, K. Welsher, W. S. Seo, W. Zhao, H. Dai, Selective synthesis combined with chemical separation of single-walled carbon nanotubes for chirality selection. *J. Am. Chem. Soc.* **129**, 15770–15771 (2007).
4. B. Wang, C. P. Poa, L. Wei, L.-J. Li, Y. Yang, Y. Chen, (*n*,*m*) selectivity of single-walled carbon nanotubes by different carbon precursors on Co-Mo catalysts. *J. Am. Chem. Soc.* **129**, 9014–9019 (2007).
5. B. Wang, L. Wei, L. Yao, L.-J. Li, Y. Yang, Y. Chen, Pressure-induced single-walled carbon nanotube (*n*,*m*) selectivity on Co-Mo catalysts. *J. Phys. Chem. C* **111**, 14612–14616 (2007).
6. W.-H. Chiang, R. Mohan Sankaran, Linking catalyst composition to chirality distributions of as-grown single-walled carbon nanotubes by tuning Ni_xFe_{1-x} nanoparticles. *Nat. Mater.* **8**, 882–886 (2009).
7. M. He, A. I. Chernov, P. V. Fedotov, E. D. Obraztsova, J. Sainio, E. Rikkinen, H. Jiang, Z. Zhu, Y. Tian, E. I. Kauppinen, M. Niemelä, A. O. I. Krause, Predominant (6,5) single-walled carbon nanotube growth on a copper-promoted iron catalyst. *J. Am. Chem. Soc.* **132**, 13994–13996 (2010).
8. C. Zoican Loebick, R. Podila, J. Reppert, J. Chudow, F. Ren, G. L. Haller, A. M. Rao, L. D. Pfefferle, Selective synthesis of subnanometer diameter semiconducting single-walled carbon nanotubes. *J. Am. Chem. Soc.* **132**, 11125–11131 (2010).
9. M. He, B. Liu, A. I. Chernov, E. D. Obraztsova, I. Kauppi, H. Jiang, I. Anoshkin, F. Cavalca, T. W. Hansen, J. B. Wagner, A. G. Nasibulin, E. I. Kauppinen, J. Linnekoski, M. Niemelä, J. Lehtonen, Growth mechanism of single-walled carbon nanotubes on iron–copper catalyst and chirality studies by electron diffraction. *Chem. Mater.* **24**, 1796–1801 (2012).
10. B. Liu, W. Ren, S. Li, C. Liu, H.-M. Cheng, High temperature selective growth of single-walled carbon nanotubes with a narrow chirality distribution from a CoPt bimetallic catalyst. *Chem. Commun.* **48**, 2409–2411 (2012).
11. F. Yang, X. Wang, D. Zhang, J. Yang, D. Luo, Z. Xu, J. Wei, J.-Q. Wang, Z. Xu, F. Peng, X. Li, R. Li, Y. Li, M. Li, X. Bai, F. Ding, Y. Li, Chirality-specific growth of single-walled carbon nanotubes on solid alloy catalysts. *Nature* **510**, 522–524 (2014).
12. F. Yang, X. Wang, D. Zhang, K. Qi, J. Yang, Z. Xu, M. Li, X. Zhao, X. Bai, Y. Li, Growing zigzag (16,0) carbon nanotubes with structure-defined catalysts. *J. Am. Chem. Soc.* **137**, 8688–8691 (2015).
13. F. Yang, X. Wang, J. Si, X. Zhao, K. Qi, C. Jin, Z. Zhang, M. Li, D. Zhang, J. Yang, Z. Zhang, Z. Xu, L.-M. Peng, X. Bai, Y. Li, Water-assisted preparation of high-purity semiconducting (14,4) carbon nanotubes. *ACS Nano* **11**, 186–193 (2017).
14. H. An, A. Kumamoto, H. Takezaki, S. Ohyama, Y. Qian, T. Inoue, Y. Ikuhara, S. Chiashi, R. Xiang, S. Maruyama, Chirality specific and spatially uniform synthesis of single-walled carbon nanotubes from a sputtered Co-W bimetallic catalyst. *Nanoscale* **8**, 14523–14529 (2016).
15. E. S. Penev, K. V. Bets, N. Gupta, B. I. Yakobson, Transient kinetic selectivity in nanotubes growth on solid Co–W catalyst. *Nano Lett.* **18**, 5288–5293 (2018).
16. K. V. Bets, E. S. Penev, B. I. Yakobson, Janus segregation at the carbon nanotube–catalyst interface. *ACS Nano* **13**, 8836–8841 (2019).
17. X. Zhang, B. Graves, M. D. Volder, W. Yang, T. Johnson, B. Wen, W. Su, R. Nishida, S. Xie, A. Boies, High-precision solid catalysts for investigation of carbon nanotube synthesis and structure. *Sci. Adv.* **6**, eabb6010 (2020).
18. F. Yang, H. Zhao, X. Wang, X. Liu, Q. Liu, X. Liu, C. Jin, R. Wang, Y. Li, Atomic scale stability of tungsten–cobalt intermetallic nanocrystals in reactive environment at high temperature. *J. Am. Chem. Soc.* **141**, 5871–5879 (2019).
19. H. An, A. Kumamoto, R. Xiang, T. Inoue, K. Otsuka, S. Chiashi, C. Bichara, A. Loiseau, Y. Li, Y. Ikuhara, S. Maruyama, Atomic-scale structural identification and evolution of Co-W-C ternary SWCNT catalytic nanoparticles: High-resolution STEM imaging on SiO_2. *Sci. Adv.* **5**, eaat9459 (2019).
20. Y. Wang, L. Qiu, L. Zhang, D.-M. Tang, R. Ma, Y. Wang, B. Zhang, F. Ding, C. Liu, H.-M. Cheng, Precise identification of the active phase of cobalt catalyst for carbon nanotube growth by *in situ* transmission electron microscopy. *ACS Nano* **14**, 16823–16831 (2020).
21. C. B. Pollock, H. H. Stadelmaier, The eta carbides in the Fe–W–C and Co–W–C systems. *Metall. Trans.* **1**, 767–770 (1970).
22. T. Johansson, B. Uhrenius, Phase equilibria, isothermal reactions, and a thermodynamic study in the Co-W-C system at 1150°C. *Met. Sci.* **12**, 83–94 (1978).
23. Z. G. Ban, L. L. Shaw, On the reaction sequence of WC–Co formation using an integrated mechanical and thermal activation process. *Acta Mater.* **49**, 2933–2939 (2001).
24. C. M. Fernandes, A. M. R. Senos, Cemented carbide phase diagrams: A review. *Int. J. Refract. Met. Hard Mater.* **29**, 405–418 (2011).
25. A. S. Kurlov, A. I. Gusev, *Tungsten Carbides: Structure, Properties and Application in Hardmetals* (Springer, 2013).
26. S. Helveg, C. López-Cartes, J. Sehested, P. L. Hansen, B. S. Clausen, J. R. Rostrup-Nielsen, F. Abild-Pedersen, J. K. Nørskov, Atomic-scale imaging of carbon nanofibre growth. *Nature* **427**, 426–429 (2004).

27. S. Hofmann, R. Sharma, C. Ducati, G. Du, C. Mattevi, C. Cepek, M. Cantoro, S. Pisana, A. Parvez, F. Cervantes-Sodi, A. C. Ferrari, R. Dunin-Borkowski, S. Lizzit, L. Petaccia, A. Goldoni, J. Robertson, *In situ* observations of catalyst dynamics during surface-bound carbon nanotube nucleation. *Nano Lett.* **7**, 602–608 (2007).
28. H. Yoshida, S. Takeda, T. Uchiyama, H. Kohno, Y. Homma, Atomic-scale *in-situ* observation of carbon nanotube growth from solid state iron carbide nanoparticles. *Nano Lett.* **8**, 2082–2086 (2008).
29. D.-M. Tang, C. Liu, W.-J. Yu, L.-L. Zhang, P.-X. Hou, J.-C. Li, F. Li, Y. Bando, D. Golberg, H.-M. Cheng, Structural changes in iron oxide and gold catalysts during nucleation of carbon nanotubes studied by *in situ* transmission electron microscopy. *ACS Nano* **8**, 292–301 (2014).
30. X. Huang, R. Farra, R. Schlogl, M.-G. Willinger, Growth and termination dynamics of multiwalled carbon nanotubes at near ambient pressure: An *in situ* transmission electron microscopy study. *Nano Lett.* **19**, 5380–5387 (2019).
31. K. Dembélé, M. Bahri, G. Melinte, C. Hirlimann, A. Berliet, S. Maury, A.-S. Gay, O. Ersen, Insight by *in situ* gas electron microscopy on the thermal behaviour and surface reactivity of cobalt nanoparticles. *ChemCatChem* **10**, 4004–4009 (2018).
32. M. J. Behr, K. Andre Mkhoyan, E. S. Aydil, Catalyst rotation, twisting, and bending during multiwall carbon nanotube growth. *Carbon* **48**, 3840–3845 (2010).
33. M. J. Behr, K. A. Mkhoyan, E. S. Aydil, Orientation and morphological evolution of catalyst nanoparticles during carbon nanotube growth. *ACS Nano* **4**, 5087–5094 (2010).
34. M. He, S. Zhang, Q. Wu, H. Xue, B. Xin, D. Wang, J. Zhang, Designing catalysts for chirality-selective synthesis of single-walled carbon nanotubes: Past success and future opportunity. *Adv. Mater.* **31**, 1800805 (2019).
35. L. Qiu, F. Ding, Understanding single-walled carbon nanotube growth for chirality controllable synthesis. *Acc. Mater. Res.* **2**, 828–841 (2021).
36. R. Sharma, P. Rez, M. Brown, G. Du, M. M. J. Treacy, Dynamic observations of the effect of pressure and temperature conditions on the selective synthesis of carbon nanotubes. *Nanotechnology* **18**, 125602 (2007).
37. L. Zhang, M. He, T. W. Hansen, J. Kling, H. Jiang, E. I. Kauppinen, A. Loiseau, J. B. Wagner, Growth termination and multiple nucleation of single-wall carbon nanotubes evidenced by *in situ* transmission electron microscopy. *ACS Nano* **11**, 4483–4493 (2017).
38. M. He, X. Wang, S. Zhang, H. Jiang, F. Cavalca, H. Cui, J. B. Wagner, T. W. Hansen, E. Kauppinen, J. Zhang, F. Ding, Growth kinetics of single-walled carbon nanotubes with a (2*n*, *n*) chirality selection. *Sci. Adv.* **5**, eaav9668 (2019).
39. M. Bahri, K. Dembélé, C. Sassoye, D. P. Debecker, S. Moldovan, A. S. Gay, C. Hirlimann, C. Sanchez, O. Ersen, *In situ* insight into the unconventional ruthenium catalyzed growth of carbon nanostructures. *Nanoscale* **10**, 14957–14965 (2018).
40. C. T. Koch, "Determination of core structure periodicity and point defect density along dislocations," thesis, Arizona State University (2002).
41. G. Kresse, J. Hafner, *Ab initio* molecular dynamics for open-shell transition metals. *Phys. Rev. B* **48**, 13115–13118 (1993).
42. G. Kresse, J. Furthmüller, Efficiency of ab-initio total energy calculations for metals and semiconductors using a plane-wave basis set. *Comput. Mater. Sci.* **6**, 15–50 (1996).
43. P. Wu, Y. Zhang, P. Cui, Z. Li, J. Yang, Z. Zhang, Carbon dimers as the dominant feeding species in epitaxial growth and morphological phase transition of graphene on different Cu substrates. *Phys. Rev. Lett.* **114**, 216102 (2015).
44. G. Kresse, D. Joubert, From ultrasoft pseudopotentials to the projector augmented-wave method. *Phys. Rev. B* **59**, 1758–1775 (1999).
45. J. P. Perdew, K. Burke, M. Ernzerhof, Generalized gradient approximation made simple. *Phys. Rev. Lett.* **77**, 3865–3868 (1996).
46. S. Grimme, J. Antony, S. Ehrlich, H. Krieg, A consistent and accurate *ab initio* parametrization of density functional dispersion correction (DFT-D) for the 94 elements H-Pu. *J. Chem. Phys.* **132**, 154104 (2010).
47. G. Henkelman, B. P. Uberuaga, H. Jónsson, A climbing image nudged elastic band method for finding saddle points and minimum energy paths. *J. Chem. Phys.* **113**, 9901–9904 (2000).
48. A. Togo, I. Tanaka, First principles phonon calculations in materials science. *Scr. Mater.* **108**, 1–5 (2015).
49. A. Togo, L. Chaput, I. Tanaka, G. Hug, First-principles phonon calculations of thermal expansion inTi_3SiC_2,Ti_3AlC_2, and Ti_3GeC_2. *Phys. Rev. B* **81**, 174301 (2010).
50. X. Zhao, F. Yang, J. Chen, L. Ding, X. Liu, F. Yao, M. Li, D. Zhang, Z. Zhang, X. Liu, J. Yang, K. Liu, Y. Li, Selective growth of chirality-enriched semiconducting carbon nanotubes by using bimetallic catalysts from salt precursors. *Nanoscale* **10**, 6922–6927 (2018).

Acknowledgments

Funding: This work was supported by the National Natural Science Foundation of China (grant nos. 51802316, 51927803, 52130209, 51972311, 51625203, and 52188101); JSPS KAKENHI (grant nos. JP20K05281 and JP25820336); Basic Research Project of Natural Science Foundation of Shandong Province, China (ZR2019ZD49); the Natural Science Foundation of Liaoning Province, China (2020-MS-009); Institute for Basic Science of South Korea (grant nos. IBS-R019-D1); and Chinese Academy of Sciences and the Shenyang National Laboratory for Materials Science. **Author contributions:** C.L., D.-M.T., L.Z., and Y.W. conceived and planned the research. Y.W., L.Z., and D.-M.T. carried out the experiments. Y.W. and D.-M.T. carried out the image simulations. Y.W., D.-M.T., L.Z., and C.L. performed data analysis. L.Q. and F.D. performed the DFT calculations. R.M. participated in the modification of the in situ growth system. C.-L.R. constructed the SiN_x amorphous models. Y.W., D.-M.T., L.Z., C.L., L.Q., F.D., and H.-M.C. wrote and revised the manuscript. **Competing interests:** The authors declare that they have no competing interests. **Data and materials availability:** All data needed to evaluate the conclusions in the paper are present in the paper and/or the Supplementary Materials.

Submitted 12 February 2022
Accepted 1 November 2022
Published 7 December 2022
10.1126/sciadv.abo5686

Science Advances

Growth mechanism of carbon nanotubes from Co-W-C alloy catalyst revealed by atmospheric environmental transmission electron microscopy

Yang WangLu QiuLili ZhangDai-Ming TangRuixue MaCui-Lan RenFeng DingChang LiuHui-Ming Cheng

Sci. Adv., 8 (49), eabo5686. • DOI: 10.1126/sciadv.abo5686

Science Advances (ISSN) is published by the American Association for the Advancement of Science. 1200 New York Avenue NW, Washington, DC 20005. The title *Science Advances* is a registered trademark of AAAS.